TROPICAL CYCLONE RESEARCH REPORT
TCRR **1**: 1–16 (2020)
Meteorological Institute
Ludwig Maximilians University of Munich

A case study of a tropical low over northern Australia

Hongyan Zhu[a1] and Roger K. Smith[b]
[a] *Bureau of Meteorology, Melbourne, Australia,* [b] *Meteorological Institute, Ludwig-Maximilians University, Munich, Germany*

Abstract:
We examine in some detail a low that intensified over land near the northern coast of Western Australia in January 2015. The study is based on European Centre for Medium Range Weather Forecasts (ECMWF) analyses as well as two cloud-permitting, 6-day, limited-area, forecasts using the UK Met. Office Unified Model (UM) with 4 km grid spacing. In one of the UM forecasts, the latent heat fluxes were suppressed over the land so as to assess the importance of soil moisture on the intensification of the low.
We show that the UM forecasts perform well using the ECMWF analyses as "truth", suggesting that the forecasts can be used to learn about the details of storm behaviour. Analyses of the forecasts support the results of previous studies showing that the intensification of the low over land can be interpreted in terms of the rotating-convection paradigm intensification articulated in recent studies. The forecasts indicate also that high soil moisture or special soil types are not essential to vortex intensification over land, at least in a monsoonal environment.

KEY WORDS Tropical low; tropical depression; monsoonal low

Date: January 30, 2020

1 Introduction

Tropical low pressure systems that occur during the "Wet" season over the northern part of the Australian continent are a major source of monsoonal rainfall and frequently lead to major flooding. Some of these lows originate from tropical cyclones after they make landfall, but when the monsoon trough lies close to the coast or over the continent, lows typically develop within the trough and intensify as they move inland and polewards. Because of the forecasting challenges posed by such systems, an improved understanding of their structure and behaviour would seem desirable. In particular, an understanding of how such lows intensify as they move inland is called for. An early study of tropical cyclogenesis in the Australian region is provided by McBride and Keenan (1982).

Some years ago, Emanuel *et al.* (2008) hypothesized that inland intensification of lows over the northern part of the Australian continent is made possible by the special type of sandy soils that are found there. These soils are argued to become hot prior to rain and are such that their thermal conductivity is greatly enhanced after being moistened by the first rains of an approaching storm so that they are able to supply sufficient surface enthalpy fluxes to support storm intensification. The ideas were demonstrated in simulations using a simple, coupled soil-atmosphere model applied to Tropical Cyclone Abigail (2001) that made landfall from the Gulf of Carpentaria and appeared to undergo two cycles of re-intensification as it progressed over land. However, the question remains as to whether this special soil type is crucial to the intensification of real storms?

In a related study, Evans *et al.* (2011) carried out numerical simulations of tropical cyclone Erin (2007), which made landfall from the Gulf of Mexico and re-intensified over the central United States. Their analysis showed, inter alia, that the along-track rainfall feedback mechanism proposed by Emanuel *et al.* was 'of minimal importance to the evolution of the vortex'. Instead, they found that 'the final intensity of the simulated (and presumably observed) vortex appears to be closely linked to the maintenance of boundary-layer moisture over pre-existing near-climatological soil moisture content along the track of the vortex and well above climatological soil moisture content'. They argued that 'variations in soil moisture content result in impacts upon the boundary-layer thermodynamic environment via boundary-layer mixing. Greater soil moisture content results in weaker mixing, a shallower boundary layer, and greater moisture and instability. Differences in the intensity of convection that develops and its accompanying latent heat release aloft result in greater warm core development and surface vortex intensification within the simulations featuring greater soil moisture content'.

Tang *et al.* (2016) carried out numerical simulations of a low that formed near the north coast of Australia during the Tropical Warm Pool International Cloud Experiment (TWP-ICE) in January 2006 (May *et al.* 2008). This low passed over Darwin, which was the focal point for the experiment, before it moved inland and intensified while moving southwards over several days. At the time of its formation, the low was well sampled by a network of radiosonde soundings in the Darwin region. Although the intensification took place over a relatively

[1]Correspondence to: Dr. Hongyan Zhu, Bureau of Meteorology, 700 Collin Street, Melbourne, Australia. E-mail: hongyan.zhu@bom.gov.au

data-sparse region of the Northern Territory, the continued data provided by the experiment should have benefited global model analyses of the low even as it moved away from the network.

Seven simulations of the low were carried out using the Pennsylvania State University, National Center for Atmospheric Research Mesoscale Model (MM5): a control simulation, five sensitivity simulations in which the initial moisture availability is varied, and one simulation in which the coupling between moisture availability is suppressed. Changing the initial moisture availability adds a stochastic element to the development of deep convection. All the simulations captured the inland intensification of the low that was seen also in the European Centre for Medium Range Weather Forecasts (ECMWF) analyses for the event.

The results of these simulations were interpreted in terms of the classical axisymmetric paradigm for tropical cyclone intensification with recent modifications, the so-called rotating-convection paradigm (see e.g. Smith and Montgomery 2016, Montgomery and Smith 2017). In essence, spin-up over land is favoured by the development of deep convection near the centre of the low circulation. As for tropical cyclones over sea, this convection leads to an overturning circulation that converges absolute vorticity in the lower troposphere. This convergence leads by Stokes' theorem to an increase of the circulation about circuits of fixed radius above the boundary layer moving with the storm and thereby to a spin-up of the tangential winds there (see e.g. Montgomery and Smith 2017: see section 4.1 and references therein).

Recently, a series of case studies based on ECMWF analyses examined the formation and evolution of such lows (Smith *et al.* 2015, Kilroy *et al.* 2016, 2017). The upshot of these studies suggested that the lows are warm-cored, convectively-driven systems, similar in structure to tropical cyclones. The fact that inland intensification the ECMWF analysis and forecast system and in the MM5 model used by Tang *et al.* (2016), which do not represent the special soil types hypothesized to be necessary by Emanuel *et al.*, supports the finding of Evans *et al.* that the along-track rainfall feedback mechanism proposed by Emanuel *et al.* is at most of minimal importance in real storms.

One limitation of the ECMWF analyses for investigating the detailed evolution of lows is the limited temporal resolution as the analyses are available only every six hours. Another limitation is the fact that the ECMWF forecast system that contributes to the analyses used a parameterization of deep convection.

In this paper we examine in some detail an inland low that formed over land near the northeastern coast of Western Australia in January 2015 and intensified as it moved inland. A visible satellite image of the low at 00 UTC 8 January 2015 is shown in Figure 1, close to the time it had reached its mature stage.

Because conventional upper-air data in the region are sparse, our study is based on ECMWF analyses as well as two cloud-permitting forecasts using the UM high resolution model with 4 km grid spacing. Questions to be addressed include: How well does UM perform using the ECMWF analyses as "truth", what can we learn about the storm behaviour from the UM forecasts and how important is high soil moisture for the intensification of the low?

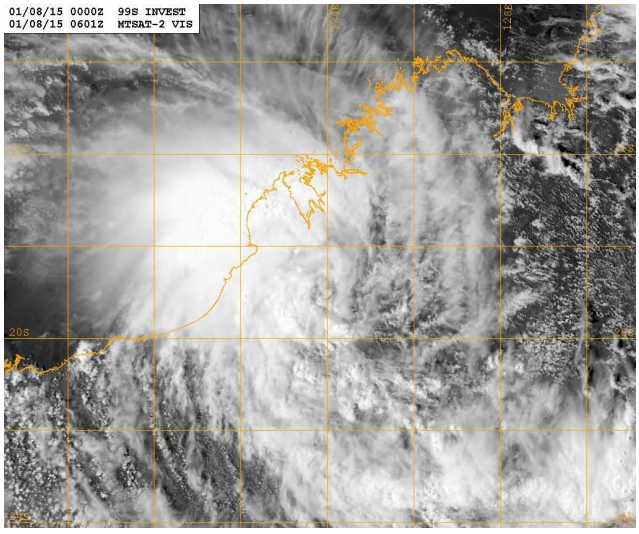

Figure 1. Visible satellite image of the low at 00 UTC 8 January 2015. Courtesy Naval Research Laboratory.

2 Broadscale synoptic setting

The ECMWF analyses are used here to provide a broadscale synoptic setting for the low. The analyses are obtained from a global 4DVAR analysis and prediction system (see e.g. Bauer *et al.* 2011). Forecasters consider the predictions from the ECMWF system to be as good as any available. The analyses are provided at the surface and at 25 pressure levels between 1000 mb and 1 mb and at 6 h intervals. The data examined here cover the domain from 100^{o}E to 160^{o}E and from 40^{o}S to 40^{o}N, with a horizontal grid spacing of 0.125^o latitude and longitude.

Figure 2 shows the wind fields at 850 mb over the foregoing domain at 00 UTC on 2 January 2015, several days before the development of the low, and at 00 UTC on 7 January when the low had developed, but had not quite reached its maximum intensity. A prominent features of the broadscale flow on 2 January (Figure 2a) is the band of strong easterlies between about 8^{o}N and 15^{o}N. These merge with a "northeasterly surge" emanating from a region to the east of China and extending over the South China Sea and for some distance to the east of the Philippines. The easterlies turn to northerlies between about 100^{o}E and 120^{o}E, crossing the equator and feeding into strong westerlies south of the equator, which are typical features of the Australasian monsoon. Indeed, these westerlies turn clockwise between about 125^{o}E and 135^{o}E to enhance an easterly flow across the northwestern part

of the Australian continent. It was within this clockwise-turning flow, cyclonic in the southern hemisphere, that the low of interest developed.

Five days later (Figure 2b), the nascent circulation over northwestern Australia seen in panel (a) has expanded and deepened to form an almost continental-scale cyclonic, monsoonal circulation centered on the low of interest. Figure 3 shows the absolute vorticity at 850 mb on 2 and 7 January in the region south of the equator in the vicinity of the low. It shows, as expected, the monsoon trough region to be one of enhanced cyclonic vorticity that provides the necessary background vorticity source for low development. What is required then is a suitable distribution of deep convection within this region that can lead to a concentration of the vorticity.

Figure 3a shows the existence of a nascent low on 2 January with its centre just onshore on the northern coast of Western Australia with patches and strips of enhanced absolute vorticity within its broad circulation. This enhanced low-level vorticity is presumably a result of the stretching of background vorticity by deep convection within the circulation (Hendricks *et al.* 2004, Montgomery *et al.* 2006, Wissmeier and Smith 2011). By 7 January (Figure 3b), the patches of enhanced vorticity have become more extensive and, as characterized by the geopotential contours, the low has intensified markedly while still centred over land. In subsequent sections, the details of the intensification will be examined in the context of forecasts using the UM model described in section 3.

Figure 4 shows the temperature distribution at 850 mb together with the geopotential and wind vectors at this level. The highest temperatures lie to the west of the low indicating that the Western Australian heat low is not directly involved in the low dynamics, even though it might account for the extension of the trough to the west of the low.

3 Model forecasts

The forecasts are carried out using the latest Regional Atmosphere and Land model developed at UK Meteorological Office (Bush *et al.* 2019).

The model dynamical core uses a semi-implicit and semi-Lagrangian formulation to solve the nonhydrostatic, fully-compressible deep-atmosphere equations of motion (Wood *et al.* 2014). The equations are solved on a limited area domain with lateral boundary conditions provided by Met. Office global model. These boundary conditions are implemented using a relaxation blending method (Davies, 1976; Perkey and Kreitzberg, 1976).

The SOCRATES radiative transfer scheme (Edwards and Slingo, 1996; Manners *et al.* 2018) is used with a configuration based on Met. Office Global Atmosphere Model (Walters *et al.* 2011).

The microphysics scheme used is a single moment scheme based on that of Wilson and Ballard (1999), with extensive modifications. The warm rain scheme is based on that of Boutle *et al.* (2014b) and includes an explicit representation of the effect of sub-grid variability on autoconversion and accretion rates (Boutle *et al.* 2014a). Ice cloud parametrisations use the generic size distribution of Field *et al.* (2007) and mass-diameter relations of Cotton *et al.* (2013).

The model uses the prognostic cloud prognostic condensate (PC2) cloud scheme (Wilson *et al.* , 2008). PC2 calculates sources and sinks of cloud cover and condensate and advects the updated cloud fields. Comparing to the diagnostic Smith cloud scheme (Smith 1990), PC2 scheme allows a cloud to deplete its liquid water content while maintaining high cloud cover.

The model atmospheric boundary layer uses blended boundary-layer parametrisation described by Boutle *et al.* (2014b). The method blends a conventional boundary layer parameterization (Lock *et al.* 2000), with a subgrid turbulence scheme suitable for large-eddy simulation. The key parameter for blending the schemes is the ratio of grid length to boundary layer depth. The scheme provides a seamless transition from parameterized to resolved turbulence.

Exchanges of mass, momentum and energy between the atmosphere and the underlying land and sea surfaces are incorporated using the community land surface model JULES (Best *et al.* 2011; Clark *et al.* 2011).

The convection parameterization scheme is switched off in this model and the convective clouds are explicitly represented by the model dynamics and thermodynamics.

The model integrated for six days with the initial condition downscaled from the driving Met. Office global model at 03 UTC on 5 January 2015. The model horizontal grid spacing is 4 km and there are 80 vertical levels with the finest resolution in the boundary layer. The domain has 600 grid points in both horizontal directions.

The comparison of intensity between the UM forecast and the analyses is remarkably close for the entire duration of the forecast. The intensity in the forecast is marginally larger than that in the analyses as would be expected as the forecasts were from a system with higher spatial resolution than the analyses. Note the regular fluctuations in intensity in both analyses and forecasts. These are a reflection of the semi-diurnal atmospheric tide that has a large amplitude in the Tropics.

4 Results

4.1 Track and intensity

Figure 5 compares the tracks of the two UM forecasts with those from the ECMWF analyses and Figure 6 compares the intensities. The low centre is defined as the location of the minimum geopotential at 850 mb, Z_{min}, and the intensity as the value of Z_{min}. The tracks in the ECMWF analyses show a small loop starting on 1 January followed

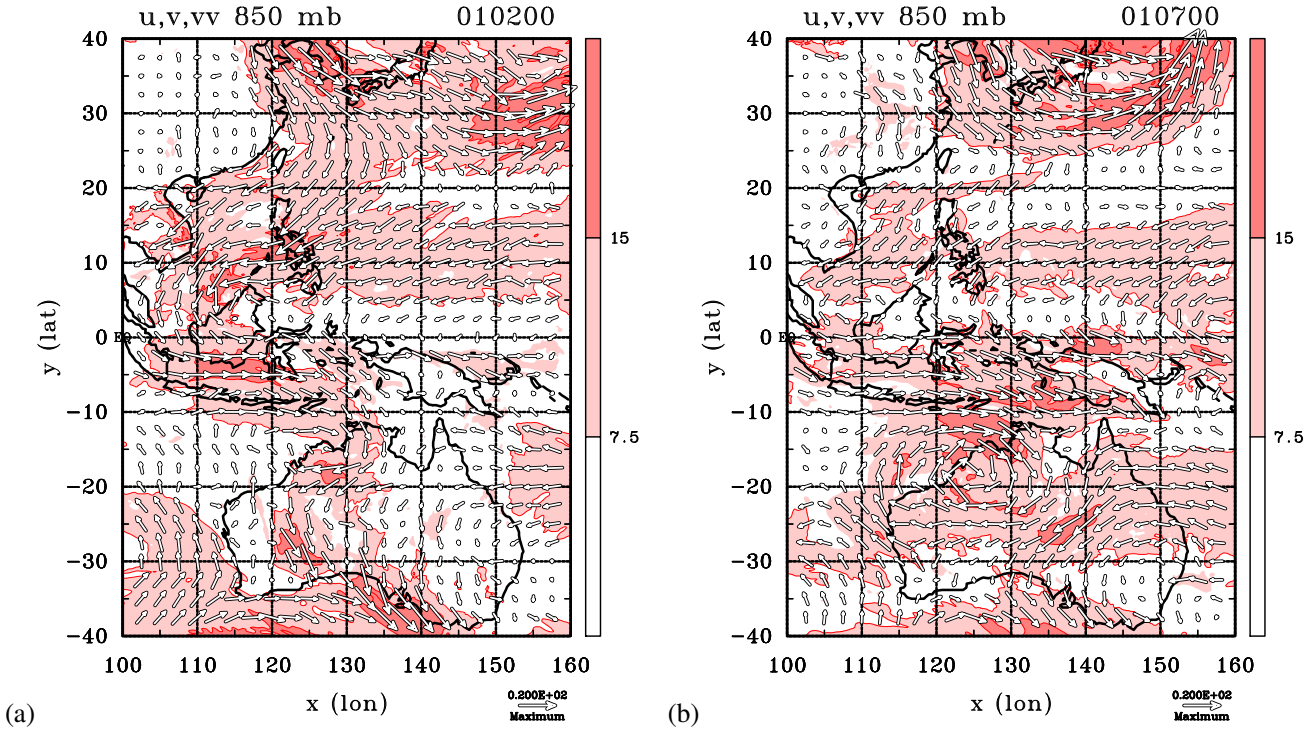

Figure 2. Wind vectors and wind speed (shaded) taken from the ECMWF analyses at 850 mb at 00 UTC on (a) 2 January and (b) 7 January 2015. Shading for wind speed as indicated in m/sec on the colour bar. Wind vector scale in m s^{-1} indicated by the arrow below the figure.

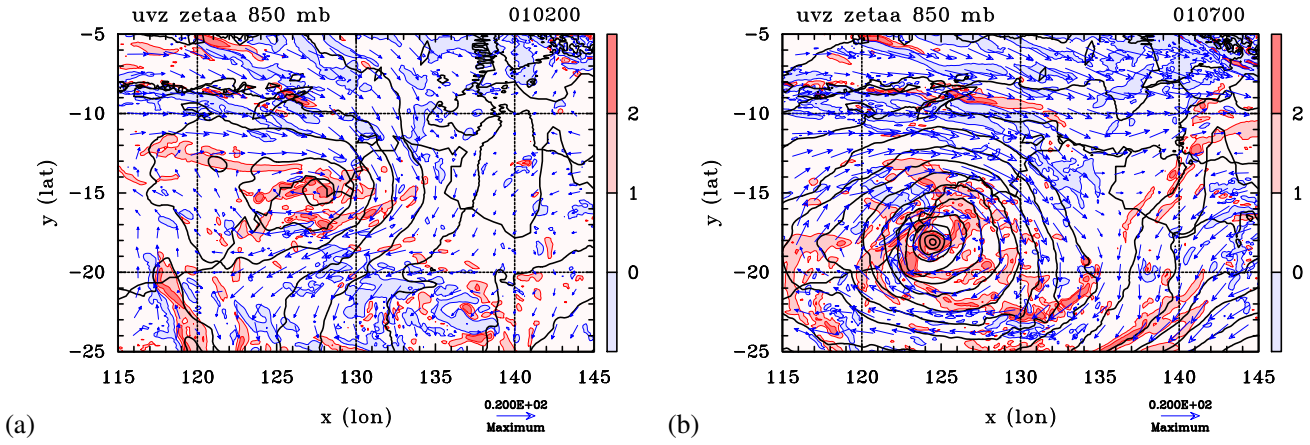

Figure 3. Wind vectors (blue arrows), geopotential (black contours, contour interval 10 m) and minus the absolute vorticity (shaded as indicated on the colour bar with interval $\times 10^{-5}$ s^{-1} at 850 mb from the ECMWF analyses at 00 UTC on (a) 2 January and (b) 7 January 2015. Wind vector scale in m s^{-1} indicated by the arrow below the figure.

a general southwestwards movement until about 8 January, when the low began to track east-southeastwards, then eastwards from 06 UTC on 10 January and northeastwards from 06 UTC on 11 January. The UM forecasts begin at 03 UTC on 5 January. Like the ECMWF analyses, the track of the low centre shows little systematic movement until sometime on 8 January, when the centre began to track a little south of east as in the analyses. After five days, the tracks in the UM forecast begins to deviate from the analysed track with a more southwards movement.

4.2 Dynamics of spin up

4.2.1 The rotating-convection paradigm

As discussed, for example, in Kilroy *et al.* (2016), the intensification of tropical lows over land can be illustrated in the context of the rotating-convection paradigm for tropical cyclone intensification over the sea as the dynamics are much the same. The dynamics of this paradigm are encapsulated, in part, by the azimuthal-mean tangential momentum equation (Persing *et al.* 2013), or equivalently by the

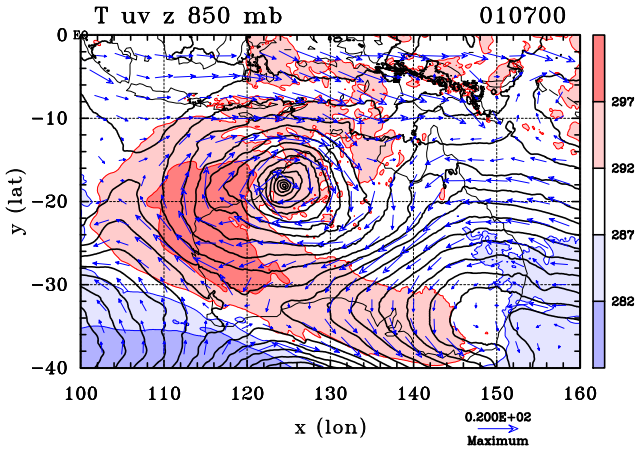

Figure 4. Wind vectors (blue arrows), geopotential (black contours, contour interval 10 m) and temperature (shaded as indicated on the colour bar, contour interval 5 K) at 850 mb from the ECMWF analysis at 00 UTC on 7 January.

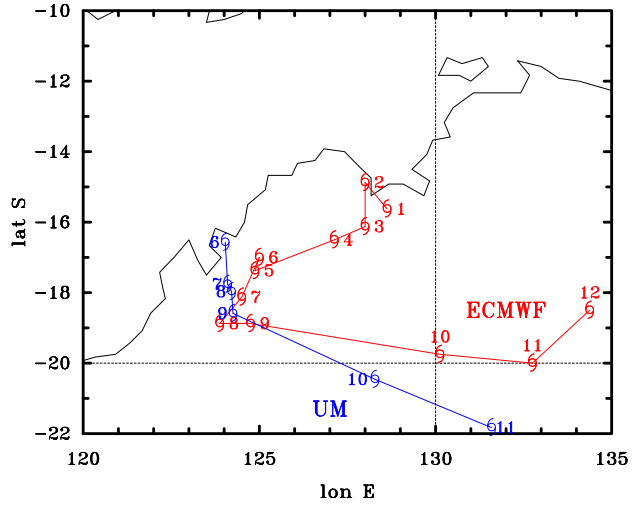

Figure 5. Comparison of tracks, as characterized by the six-hourly locations of the minimum geopotential at 850 mb, Z_{min}, between the UM forecast with 4 km grid spacing (blue) and the ECMWF analyses (red). Numbers refer to 00 UTC on the January day indicated and locations are marked by a cyclone symbol.

vertical vorticity equation in conjunction with Stokes' theorem (Montgomery and Smith, 2017, section 4.1). This theorem equates the circulation about any fixed loop to the area integral of the vorticity within that loop. While the spin up tendency derived directly from the tangential momentum equation and that inferred indirectly from the vorticity equation in conjunction with Stokes' theorem are mathematically equivalent, the vorticity approach leads arguably to greater insights, especially in relation to the effects of the generation of local rotation by convection. For this reason, the main focus here is on the vorticity approach.

The rotating-convection paradigm recognizes the need for a modest elevation of surface enthalpy fluxes to maintain deep convective instability in the inner core region

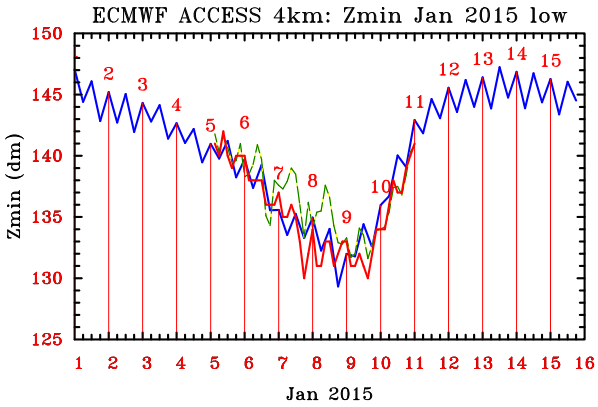

Figure 6. Comparison of intensities as characterized by the minimum geopotential at 850 mb, Z_{min}, between the ECMWF analyses (blue), the UM forecast with 4 km grid spacing (red) and a UM forecast in which the surface latent heat flux is set to zero over land (yellow/green dashed).

of the vortex, which is required for continued intensification of the vortex (Montgomery and Smith, 2017, p551). Moreover, the paradigm relates to vortex evolution in three-dimensions, which is arguably the proper benchmark for interpreting observations and numerical model simulations of tropical cyclones.

4.2.2 Flux form of the vorticity equation

In pressure coordinates, the equation for the local tendency of the vertical component of absolute vorticity, ζ_a, has a particularly concise form in terms of a *horizontal* divergence of a *horizontal* flux (Haynes and McIntyre, 1987), i.e.,

$$\frac{\partial \zeta_a}{\partial t} = -\nabla_h \cdot \mathbf{F}_{\zeta_\mathbf{a}}, \qquad (1)$$

where $\mathbf{F}_{\zeta_\mathbf{a}} = \mathbf{F_{af}} + \mathbf{F_{naf}}$, with $\mathbf{F_{af}} = \zeta_a \mathbf{u_h}$, and $\mathbf{F_{naf}} = -\zeta_\mathbf{h}\omega + \mathbf{k} \wedge \mathbf{F_{fri}}$. Here $\mathbf{u_h} = (u, v, 0)$ is the horizontal velocity vector, $\zeta_\mathbf{h}$ is the horizontal component of vorticity, ω is the material derivative of pressure and plays the role of 'vertical velocity' in pressure coordinates, $\mathbf{F_{fri}}$ is the horizontal force per unit mass due to molecular effects and subgrid-scale eddy momentum fluxes, and $\mathbf{k}$ is a unit vector in the vertical. Equation (1) applies equally to rectangular coordinates (x, y, p) or cylindrical coordinates (r, λ, p), in which r is the radius, λ is the azimuth and u and v are the radial and tangential velocity components. Raymond *et al.* (2014) provide a succinct interpretation of the terms in Equation (1): see their Fig. 1 and related discussion. The flux vectors $\mathbf{F_{af}}$ and $\mathbf{F_{naf}}$ are called the *advective flux* and *non advective flux*, respectively. Above the boundary layer, where $\mathbf{F_{fri}}$ can be neglected, the *non-advective flux*, $\mathbf{F_{naf}}$, incorporates the effects of vertical vorticity advection and the tilting of horizontal vorticity into the vertical that appear separately in the material form of the vorticity equation.

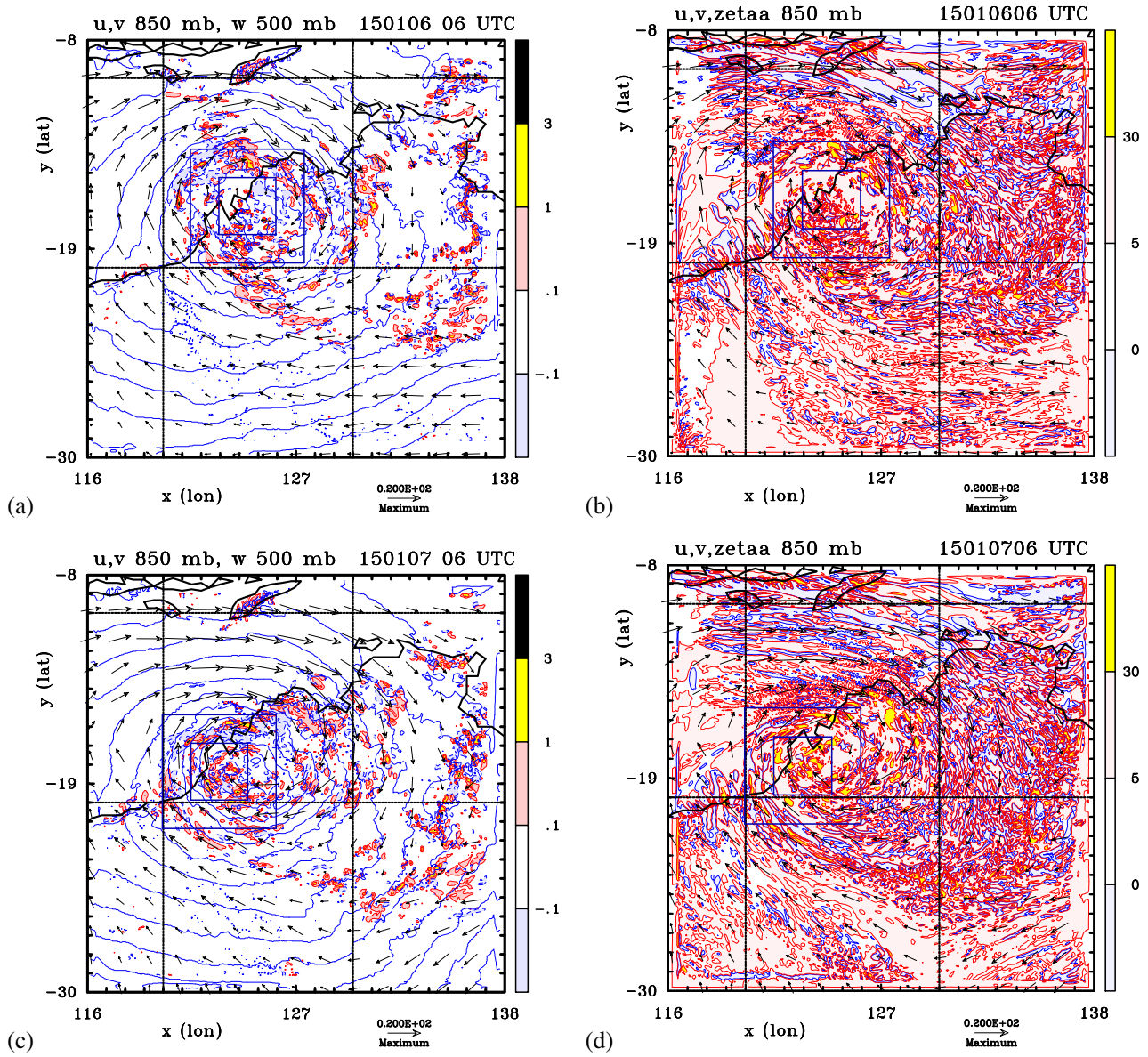

Figure 7. Vertical velocity fields at 500 mb (left columns, colour shaded) and minus the absolute vorticity fields at 850 mb (right columns, colour shaded) with the wind fields and geopotential at 850 mb superimposed from the 4 km grid UM forecast at selected times: (a),(b) 0600 UTC 6 January, (c),(d) 0600 UTC 7 January. Contour intervals: for vertical velocity as indicated on the colour bar in m s^{-1}; for absolute vorticity as indicated on the colour bar in $\times 10^{-5}$ s^{-1}.

4.2.3 Axisymmetric flow

For an axisymmetric flow, $\mathbf{F_{af}}$ reduces to $u\zeta_a\hat{\mathbf{r}}$ and, above the frictional boundary layer, $\mathbf{F_{naf}}$ reduces to $\omega(\partial v/\partial p)\hat{\mathbf{r}}$, where $\hat{\mathbf{r}}$ is a unit vector in the radial direction. In this case, the vorticity equation has the flux form

$$\frac{\partial \zeta_a}{\partial t} = -\frac{1}{r}\frac{\partial}{\partial r}\left[r\left(u\zeta_a + \omega\frac{\partial v}{\partial p}\right)\right], \qquad (2)$$

which is equivalent to the perhaps more familiar material form:

$$\frac{\partial \zeta_a}{\partial t} + u\frac{\partial \zeta_a}{\partial r} + \omega\frac{\partial \zeta_a}{\partial p} = \zeta_a\frac{\partial \omega}{\partial p} - \frac{\partial v}{\partial p}\frac{\partial \omega}{\partial r}, \qquad (3)$$

in which the left-hand-side is just the material derivative of ζ_a and the terms on the right-hand-side represent the generation of vorticity by the vertical stretching of existing ζ_a and the tilting of radial vorticity (proportional to $\partial v/\partial p$) by the radial gradient of ω.

Above the boundary layer in a warm-cored vortex, the tangential velocity decreases with altitude so that the non-advective flux vector points outwards. It follows that tilting by a convectively-driven, axisymmetric overturning circulation would lead to enhanced cyclonic vorticity at radii where the vertical velocity increases with radius, i.e., where $\partial\omega/\partial r < 0$, and reduced vorticity at larger radii where $\partial\omega/\partial r > 0$. Within the boundary layer, $\omega(\partial v/\partial p)\hat{\mathbf{r}}$ points inwards and the vorticity tendencies due to tilting are

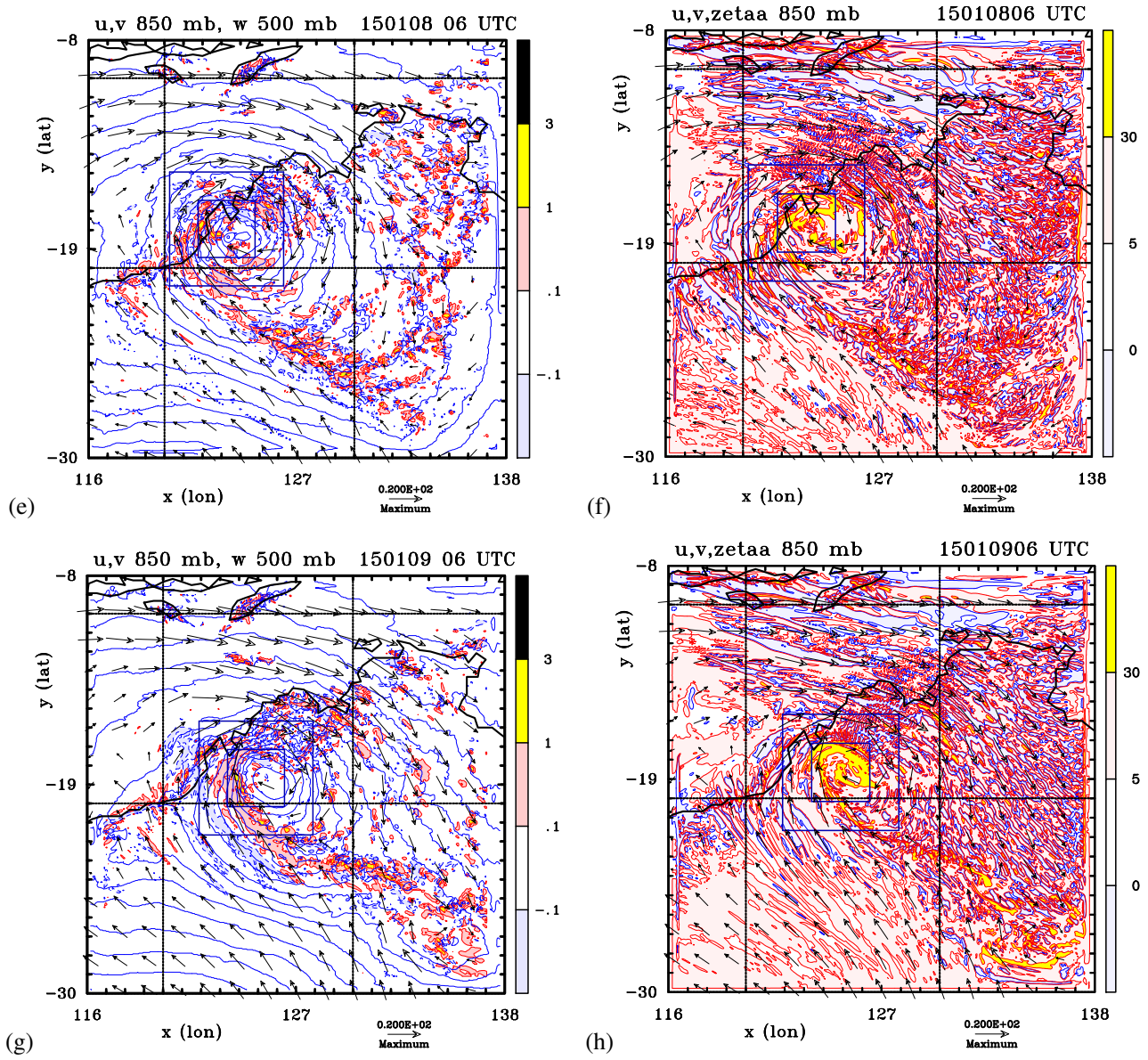

Figure 7. (continued) panels for times: (e),(f) 0600 UTC 8 January, (g),(h) 0600 UTC 9 January.

reversed in sign, but there one cannot, of course, ignore the contribution of $\mathbf{F}_{\mathbf{fri}}$ to $\mathbf{F}_{\mathbf{naf}}$ (see Raymond *et al.* 2014, Fig. 1c).

The corresponding axisymmetric, inviscid, isobaric, tangential momentum equation[1] has the form:

$$\frac{\partial v}{\partial t} = -u\zeta_a - \omega\frac{\partial v}{\partial p}. \qquad (4)$$

Since $\zeta_a = (1/r)\partial M/\partial r$, where $M = rv + \frac{1}{2}fr^2$ is the absolute angular momentum, the term $u\zeta_a$ is proportional to the radial advection of M and characterizes the local spin up or spin down that occurs as air parcels move radially while conserving their value of M. In essence, *this term represents the classical spin up mechanism* articulated by Ooyama (1969): see Montgomery and Smith (2014). The term $\omega(\partial v/\partial p)$ is proportional to the vertical advection of M. Note further that the two terms on the right-hand-side of (4) are just the advective and non-advective fluxes, respectively, that appear on the right-hand-side of Eq. (2).

[1]It is easy to verify that the divergence $(1/r)\partial[r \times Eq.\,(4)]/\partial r$ leads to Eq. (2).

4.2.4 Non-axisymmetric flow

In a flow that is not axisymmetric, one can consider the change in circulation about a fixed circular loop at a given pressure level and radius. By Stokes' theorem, the circulation at a particular time is equal to the areally-integrated vorticity within the loop. Hence, the circulation about the loop will increase if there is a mean flux of positive absolute vorticity into the loop. In Equation (1), which is not

restricted to axial symmetry, the convergence of the advective flux incorporates the effects of both the radial vorticity advection and the stretching of vertical vorticity, terms that appear separately in the corresponding material form of the vorticity equation. Since the circulation about the loop is proportional to the mean tangential velocity around the loop, an increase in circulation implies an increase in the mean tangential wind speed at this radius. The rotating-convection paradigm invokes the lower tropospheric branch of the overturning circulation produced by the collective effects of deep convection within the loop to provide the influx of vorticity required for vortex intensification.

On the convective scale, where the flow is fully three-dimensional, the non-advective flux leads to localized vorticity dipoles (Kilroy and Smith, 2015). If a particular convective element occurs entirely within some circular loop in a pressure surface, the associated vorticity dipole will not contribute to the circulation about the loop. For this reason, only dipoles that are intersected by a particular loop would contribute to the circulation about that loop. Dipoles that are contained entirely within the loop do not contribute. Therefore, the main contribution to the non-advective flux is from the azimuthally-averaged vortex-scale dipole discussed in section 4.2.3 for the pure axisymmetric case.

4.2.5 Tangential wind tendency

The alternative approach to investigating spin up for the case of non-axisymmetric vortex is to use an azimuthally-averaged form of the tangential momentum equation:

$$\frac{\partial < v >}{\partial t} = - < u\zeta_a > - < \omega \frac{\partial v}{\partial p} >, \qquad (5)$$

where the brackets $< >$ denote an azimuthal average at a fixed radius and height centred on an appropriate definition of the vortex centre. Typically, quantities on the right-hand-side of this equation would be separated into azimuthal mean terms and terms involving perturbations about this mean leading to so-called "eddy contributions" to spin up. The eddy terms complete the description of the spin up process by accounting for the effects of localized deep convection. As in the axisymmetric form (Eq. (4)), comparison between (5) and (1) indicates that the two terms on the right-hand-side of (5) are just the advective and non-advective fluxes, respectively, that appear on the right-hand-side of Eq. (1).

As explained above, the main contribution to the non-advective flux is from the azimuthally-averaged vortex-scale dipole. This equivalent effect is contained in the second term on the right-hand-side of Equation (5) as a vertical flux of tangential momentum. This effect is a particularly important element of eyewall spin up because the vorticity flux $- < u\zeta_a >$ in the eyewall is outwards on account of the outward radial flow there (Persing *et al.* 2013, Smith and Schmidt 2016).

The alternative articulation of the rotating-convection paradigm framed in terms of the azimuthally-averaged momentum equations is discussed in detail by Persing *et al.* (2013) and reviewed by Montgomery and Smith (2017, section 4.2). Its extension to encompass the effects of vertical shear is discussed by Smith *et al.* (2017).

4.2.6 Vorticity analysis of the UM forecast

Figure 7 shows a sequence of flow fields taken from the UM forecast at selected times during the intensification period. These fields include vertical velocity fields at 500 mb and absolute vorticity fields at 850 mb. In each case, the wind vectors at 850 mb are superimposed.

The left panels of Figure 7 show the vertical velocity fields at 500 mb, which give an indication of regions with deep convective cells (the yellow areas represent updraughts in excess of 1 m s^{-1} and the black regions within these cells are where the updraughts exceed 4 m s^{-1}. At 0600 UTC 6 January (panel (a)), there are numerous cells of deep convection within the broadscale circulation of the low, but only one or two cells within a degree of the circulation centre. At this time, which is close to the time of diurnal convection maximum over land (Yang and Slingo, 2001), much of the convection is located several degrees away from the centre. By 7 January (panel (b)), however, the low has intensified and deep convective cells have begun to develop closer to the circulation centre. The latter location is a geometrically favourable for continued intensification because the convectively-induced secondary circulation is able to concentrate absolute vorticity close to the centre (see Smith and Montgomery, 2016, especially section 3.2).

One day later, at 0600 UTC 8 January, near the time of maximum intensity in the UM forecast (Figure 3), there are some intense convective cells in the sector from west to north of the circulation centre, but again much of this convection is located several degrees from the centre, a situation that is not conducive to further development.

The intensification of the low occurred in a favourable cyclonic vorticity-rich environment of the monsoon trough (Figure 7, right column). Large areas of this environment have embedded small-scale anticyclonic vorticity anomalies that are presumably a result of the tilting of horizontal vorticity into the vertical. Such a process leads to vorticity dipoles (see e.g. Kilroy and Smith 2016). The large cyclonic absolute vorticity anomalies are produced by the vertical stretching of absolute vorticity, principally by moderate to deep convection (Hendricks *et al.* 2004, Wissmeier and Smith 2010).

At 0600 UTC 6 January, the enhanced cyclonic absolute vorticity anomalies (regions coloured yellow in the right column of Figure 7), are patchy, but are distributed over a large area of the incipient low vortex. However, as time proceeds, patched nearest to the centre aggregate to form an approximate monopole structure in the central region of the vortex (Figure 7h). It is this process of vorticity aggregation in the lower troposphere that leads to the

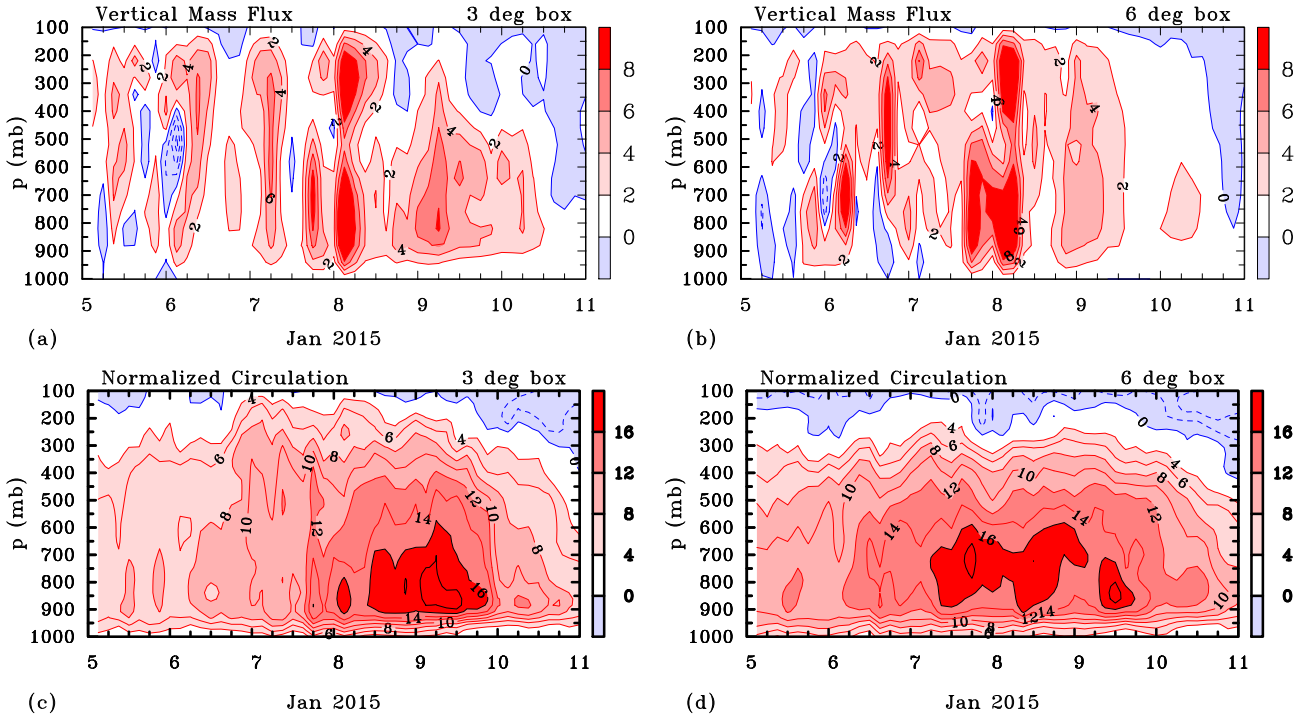

Figure 8. Time-height cross-sections of system-averaged vertical mass flux per unit area (Unit: kg m^{-2} s^{-1}) within lat-lon columns (a) 3^o lat $\times 3^o$ lon, and (b) 6^o lat $\times 6^o$ lon, centred on the location of the minimum wind speed at 850 mb (Contour interval 2 units as indicated on the colour bar). Panels (c) and (d) show the corresponding time series of the magnitude of system-averaged normalized circulation (m s^{-1}) around these columns. Contour interval 2 units as indicated on the colour bar.

vortex intensification, a result of Stokes' circulation theorem. In turn, the convergence is brought about by the lower-tropospheric branch of the overturning circulation associated with the collective effects of deep convection.

Another prominent feature of the vorticity fields is the development of a band of enhanced vorticity stretching southeastwards from the low. This band is most pronounced on 8 and 9 January (Figures 7f and 7h) and is seen to be accompanied by a band of vigorous deep convection that separates a southeasterly flow of continental origin from the moist, northeasterly monsoonal flow circulating around the low.

To cement our interpretations of the convectively-induced low-level convergence leading to the concentration of absolute vorticity and thereby an increase in the low-level circulation of the vortex, we show in Figure 8 time-height cross-sections of system-averaged vertical mass flux within latitude-longitude columns 3^o latitude $\times 3^o$ longitude and 6^o latitude $\times 6^o$ longitude in cross-section, centred on the location of the minimum wind speed at 850 mb. Show also are the corresponding time-height cross-sections of normalized circulation (circulation divided by the length of the circuit) around these columns.

In the smaller area column (Figure 8a), there are regular 'bursts" of deep upward mass flux until about 0600 UTC on 9 January, a time at which the storm was near its maximum intensity (Figure 6). These bursts have a tendency to occur in the afternoon or evening (0300 UTC-1200 UTC local time) as would be expected over land. At most later times, the bursts do not extend through a deep layer.

In the larger area column (Figure 8b), the strongest bursts occur in the 12 h period starting 1800 UTC 7 January and mass flux values tend to be larger than in the smaller area column, at least until about 1200 UTC 8 January, indicating that much of the deep convection in the low lies outside the inner 3^o latitude $\times 3^o$ longitude area. Figure 7 exemplifies this behaviour at 0600 UTC 6 January (panel (a)), 8 January (panel (e)) and 9 January (panel (g)). In contrast, at 0600 UTC 7 January (Figure 7c), there is much vigorous deep convection over a substantial part of $3^o \times 3^o$ column.

Figure 8c and 8d show the evolution of the normalized circulation around the two columns with time and height. The normalized circulation around the innermost column shows a sharp increase through a deep layer starting a little before 18 UTC 7 January, but the next prominent and sustained increase occurs about 18 h later, one that is confined mostly to heights below the 700 mb level. In other words, the low is a "bottom up" development as opposed to "top down", a finding similar to that in the cases described by Kilroy *et al.* (2016, Fig. 9f) and Kilroy *et al.* (2017, Figs. 5f, 10f and 14f). Even so, the enhanced cyclonic circulation extends through most of the troposphere during the intensification and mature stages.

The normalized circulation around the $6^o \times 6^o$ column

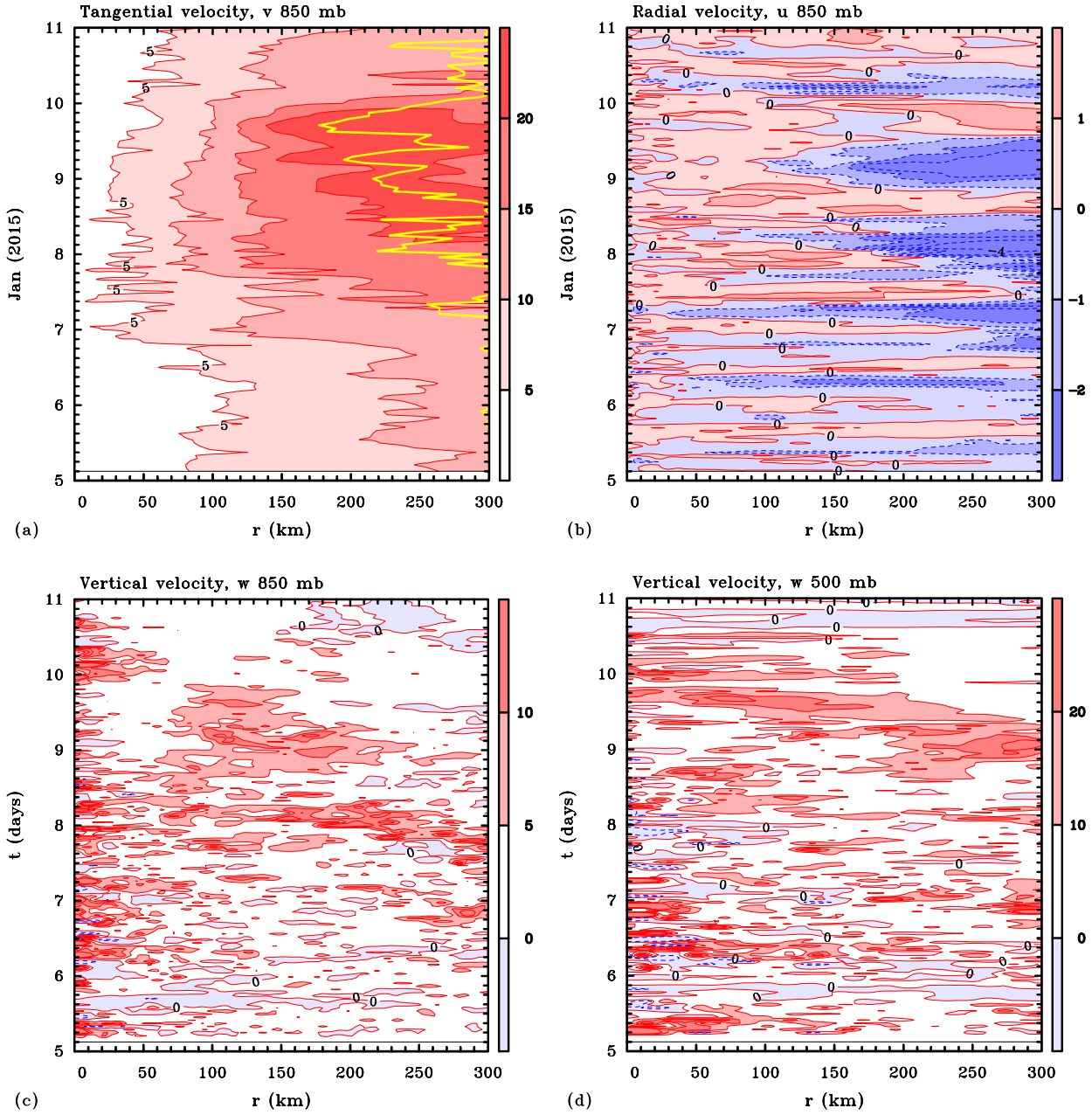

Figure 9. Hovmöller radius-time cross-sections of the (a) tangential, and (b) radial velocity components at 850 mb from the UM forecasts. Contour intervals as indicated on the colour bar in m s^{-1}. Panel (c) and (d) show similar cross-sections of vertical velocity at 850 mb and 500 mb, respectively. Contour interval 10 cm s^{-1}. Shading as indicated on the colour bar in cm s^{-1}.

shows a more prolonged enhancement, especially at pressure levels above 600 mb, with a significant increase beginning about 0900 UTC 7 January, about a day earlier than in the $3^o \times 3^o$ column, and again with maximum strength in the lower troposphere, in this case at pressure levels above 600 mb. The cyclonic circulation around this column does not extend quite so high as in the $3^o \times 3^o$ column. This feature would be expected and is consistent with the idea that as air parcels move outwards at upper levels, the Coriolis force they experience leads to a anticyclonic circulation beyond a certain radius.

Further insight into the role of convectively-induced low-level convergence in leading to an increase in the low-level vortex circulation is provided by the Hovmöller (radius-time) plots of the azimuthally-averaged radial and tangential velocity components relative to the moving vortex centre at 850 mb shown in the upper panels of Figure 9.

In general, tangential winds exceeding 20 m s^{-1} do not occur until 3 UTC 8 January, about 9 hours after the minimum geopotential (cf. Figure 6). These values are located beyond a radius of 150 km and persist until late on 9 January. The maximum tangential velocity (23.6 m s^{-1}) occurs at 15 UTC 9 January at a radius of 177 km.

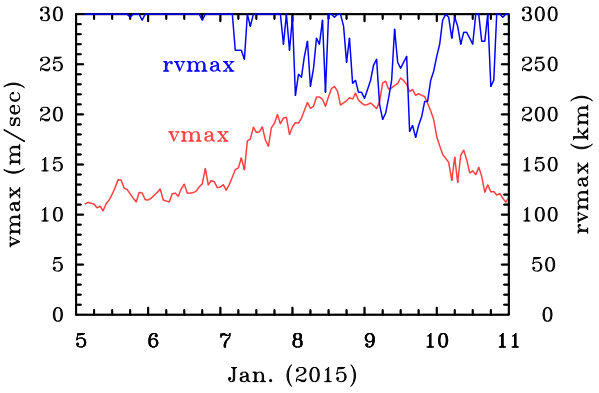

Figure 10. Time series of R_{Vmax} (corresponding with the yellow curve in Figure 9a) and V_{max} at 850 mb.

Thus, unlike a typical tropical cyclone in the region, *the low did not have a concentrated core of high rotational winds* within, say, 100 km of the centre. There were significant fluctuations in the radius, R_{Vmax}, of maximum tangential wind speed, V_{max}, as illustrated by the yellow line in panel (a).

Time series of R_{Vmax} shown in Figure 9 and the corresponding and of V_{max}, itself, are shown in Figure 10. Comparison of the curve for V_{max} with that for the minimum geopotential, Z_{min}, in Figure 6 shows that whereas the maximum intensity as measured by Z_{min} occurs at 18 UTC 7 January, the maximum intensity as measured by V_{mas} occurs nearly two days later at 12 UTC 9 January. There is not a clear relationship between changes in R_{Vmax} and changes in V_{max}: during some time periods V_{max} value of R_{Vmax} occurs 6 h later than the maximum V_{max} although changes in V_{max} are relatively small during the period.

Returning now to Figure 9, we note that there are periods where the radial flow is inwards and periods when it is outwards, but the periods of inflow become increasingly prolonged as the low intensifies and matures. The largest values of inflow (above 2 m s^{-1}) are found to occur mostly beyond a radius of 150 km from the centre of the low. On 8 January, maximum values of inflow were in excess of 4 m s^{-1}. These pulses of inflow can be attributed to the occurrence of deep convection and are suggestive that the classical paradigm for tropical cyclone intensification is operating to support the spin up of the low.

Figure 9c and 9d show the azimuthally-averaged vertical velocity at 850 mb and 500 mb, respectively. Elevated values of vertical velocity at 500 mb that are approximately colocated with such values at 850 mb provide an indication of the radial location(s) of deep convection at a particular time and radius. It is significant that, in the simulation, there are regions of deep convection within 50-100 km of the vortex centre during the spin up phase of the low ending late on 7 January (Figure 6). These regions contribute to the convective "bursts" seen in the 3^o latitude $\times 3^o$ column averages shown in Figure 8a. This location near the centre of circulation would be a geometrically favourable location for vortex intensification (Smith and Montgomery 2016). After about 18 UTC 8 September until 21 UTC 9 September, there is at most weak ascent at 850 mb within about 60 km of the vortex centre, although there is marked ascent at 500 mb after about 12 UTC 9 September. The lack of deep convection in the central region during this period is consistent with the weakening of the low.

Figure 11 shows Hovmöller (radius-time) plots of the azimuthally-averaged absolute vorticity flux and vertical tangential momentum flux, equivalent to the terms on the right-hand-side of Equation 5[2], but at a height of 1.5 km (close to the 850 mb isobaric surface). As noted in section 4.2.1, these two terms are simply the advective and non-advective vorticity fluxes that appear in the vorticity tendency equation (1). The sum of these two terms, which according to Equation (5) gives the tangential wind tendency, ignoring, of course the turbulent diffusion of tangential momentum and any eddy contributions[3], is shown in Figure 12.

During the main spin up phase of the low, between 00 UTC 7 January and 12 UTC 9 January (Figure 10), there are several notable pulses of vorticity flux: one between about 00 UTC and 09 UTC 7 January, a more prolonged one between about 15 UTC 7 January and 12 UTC 8 January and further one between about 00 UTC and 12 UTC 9 January (Figure 11a). Of course, these pulses coincide with periods of enhanced inflow. The tangential wind tendency of the last two pulses is reinforced at radii beyond about 100 km radius by a positive vertical flux of tangential momentum (Figures 11b and 12), but the absolute vorticity flux makes the dominant contribution to spin up. This finding adds support to the foregoing idea that classical paradigm for tropical cyclone intensification is operating to promote the spin up of the low.

As a point of interest, the tangential wind tendency due to the azimuthally-averaged vertical flux of tangential momentum (equivalent to the non-advective vorticity flux) is opposite to that in a tropical cyclone (see section 4.2.3) where positive values are expected at inner radii and negative values at outer radii. Here, negative values are found at inner radii and positive values at outer radii, albeit still within the radius of maximum tangential wind speed. These differences appear to be related to the relatively wide inner core region in the low and the nature of the flow asymmetries therein.

4.3 Thermodynamic aspects

4.3.1 Thermal structure

Figure 13 shows zonal and meridional cross-sections of perturbation potential temperature, θ', as a function of

[2]From the UM model output it turned out to be easier to evaluate these terms in height coordinates in which $< w\partial v/\partial z >$ replaces $< \omega\partial v/\partial p >$.

[3]A complete budget of the full azimuthally-averaged tangential momentum equation taking account of these additional terms is beyond the scope of the present study.

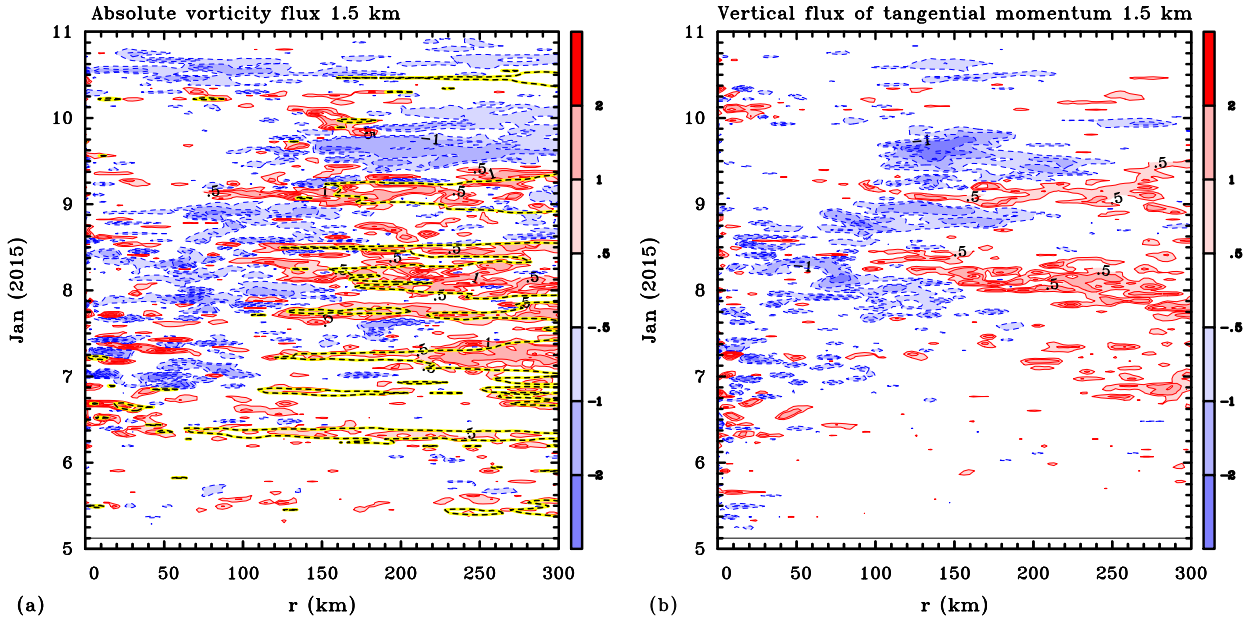

Figure 11. Hovmöller radius-time cross-sections of the azimuthally-averaged absolute vorticity flux and vertical momentum flux on the right-hand side of Equation (5) at a height of 1.5 km diagnosed from the UM model forecast. These are equivalent to the advective and non-advective vorticity fluxes that appear in Equation (1). Contour intervals as indicated on the colour bar in m s^{-1} per hour. The dashed black/yellow contours in (a) enclose regions where the inflow exceeds 1 m s^{-1}.

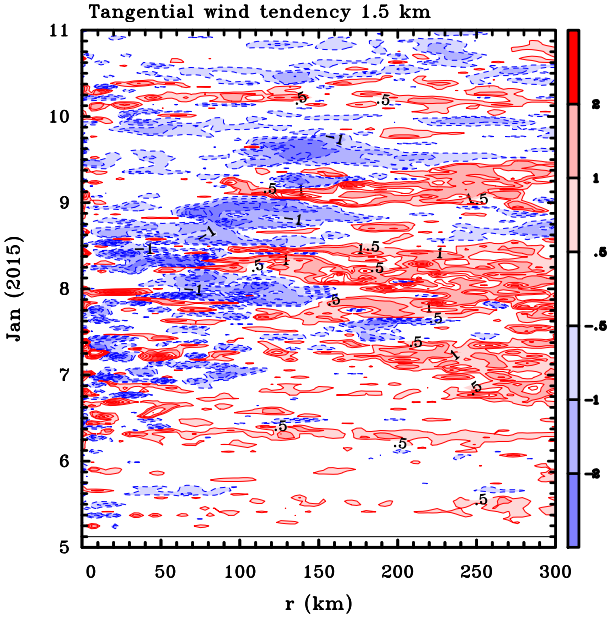

Figure 12. Hovmöller radius-time cross-sections of the azimuthal-mean tangential wind tendency, evaluated using Equation (5) as sum of the two terms in Figure 11. Contour intervals as indicated on the colour bar in m s^{-1} per hour.

height through the centre of the mature low at 0600 UTC 9 January. The perturbation is relative to a domain average of potential temperature at each pressure level. It is seen that the low has a warm core aloft ($\theta' > 0$), but is cold cored in the lower troposphere, similar that of the monsoon trough itself (Love and Garden, 1984). These latter authors surmised that the cold core structure in the lower troposphere is a result of the evaporation of precipitation in the relatively dry continental air that wraps into the monsoon on the southern and western side of the monsoon trough. The cross-sections in Figure 13 supports that idea to a degree in that the maximum cool anomalies are found on the southern and western and sides of the low where continental air would be wrapped around it. However, there is a significant cool anomaly on the northern side of the low as well, albeit more than a degree away from the centre.

4.3.2 Soil moisture and latent heat flux over land

Through much of its intensification stage, the low centre was over land, albeit not too far inland, no more than about 300 km at its most intense stage. However, it was embedded in a large-scale monsoonal circulation with abundant moisture supply to the north and west from the warm ocean, where sea surface temperatures were in excess of 29^{o}C. The immediate question that arises is whether the ocean moisture source was sufficient to support the intensification process over land, or whether soils, moistened by previous monsoonal rainfall events, were an important factor also? To set the scene for answering this question, we show in Figure 14 the distribution of soil moisture at 0300 UTC 5 January and 1800 UTC 7 January.

On 5 January, at the start of the UM simulation, the soil within 1-2^o latitude of the circulation centre was relatively moist with large patches having values exceeding 300 kg m^{-3}. The moist soils extend over much of the region shown, to the east of the low and to about 21^{o}S, while soils

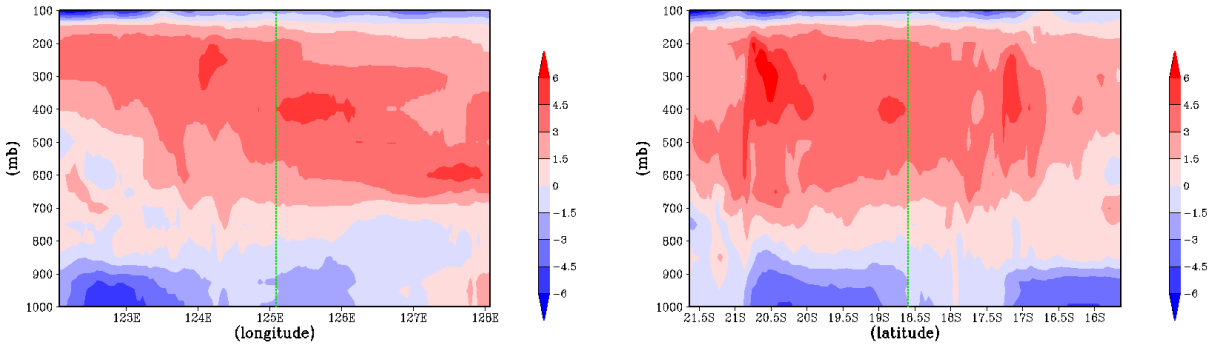

Figure 13. Vertical cross-sections of perturbation potential temperature (in K) through the low centre (125.1^{o}E, 18.6^{o}S) at 0600 UTC 9 January. The low centre is taken as the location of minimum geopotential height at 850mb and is indicated by the vertical dashed line in each panel. The perturbation is relative to the domain average at each pressure level. The zonal cross-section in (a) is at the latitude 18.6^{o}S and the meridional cross-section in (b) is at the longitude 125.1^{o}E.

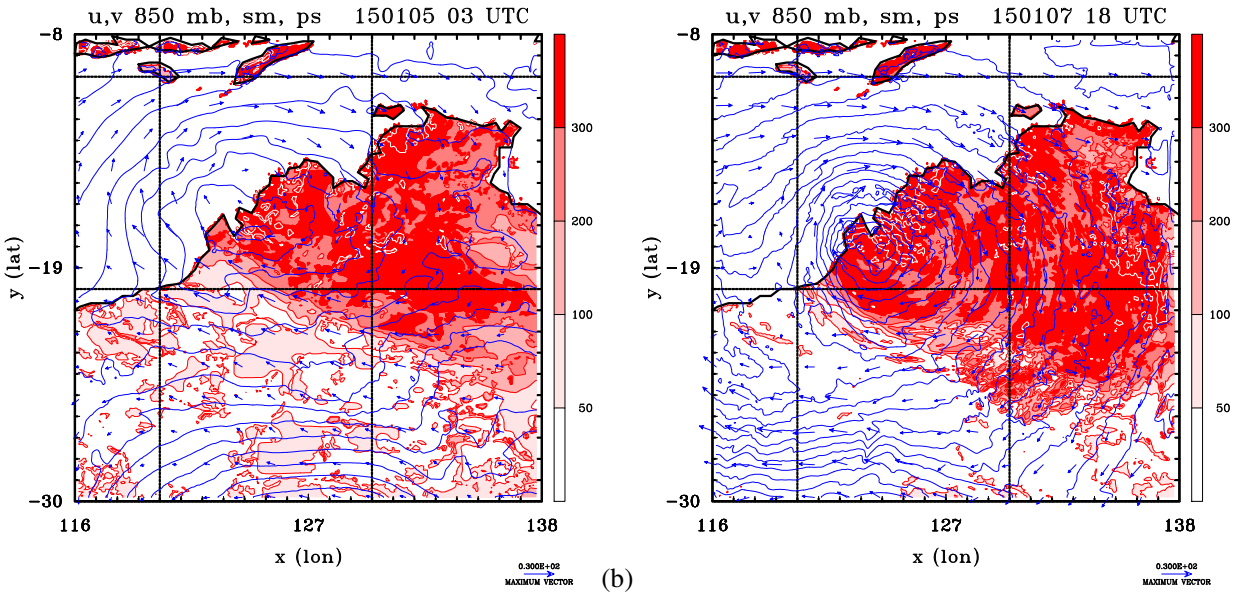

Figure 14. Distribution of soil moisture (shaded), surface pressure and wind vectors at two times: (a) 0300 UTC on 5 January, (b) 1800 UTC on 7 January. Unit for soil moisture: kg m^{-3} as indicated on the colour bar. Contour interval for surface pressure 1 mb, wind vector scale in m s^{-1} indicated by the arrow below the figure.

beyond a few degrees to the south and south west of the circulation centre are comparatively dry.

On 7 January, the region of moist soils has extended southwards and as would be expected, the moisture has increased in the vicinity of the low. On the other hand, the soils to the south and southwest have become drier.

To examine the potential influence of soil moisture on the intensification of the low, Figure 15 shows the spatial distribution of surface latent flux at 0600 UTC, when the low in the model was still strengthening, and at 1800 UTC on 7 January, times when the low first reached its peak intensity. This figure shows that latent heat fluxes have a strong diurnal variation, being a maximum during the daytime (e.g. at 0600 UTC, 2 pm local time in Western Australia) and falling to zero over night (e.g. at 1800 UTC 2 am local time). Typical values are in the range 100-200 W m^{-2}, comparable with values found by Kilroy *et al.* (2016, Fig. 10) and Kilroy *et al.* (2017, p774). Typical values over the ocean during the monsoon are somewhat higher (from 200 W m^{-2} to more than 400 W m^{-2} in the case examined by Kilroy *et al.* (2016): see their Fig. 10).

To examine further the impact of soil moisture on the intensification of the low over land, we carried out an additional simulation in which the surface latent heat flux is set to zero over land. The intensification curve for his simulation is included in Figure 6. As expected, the

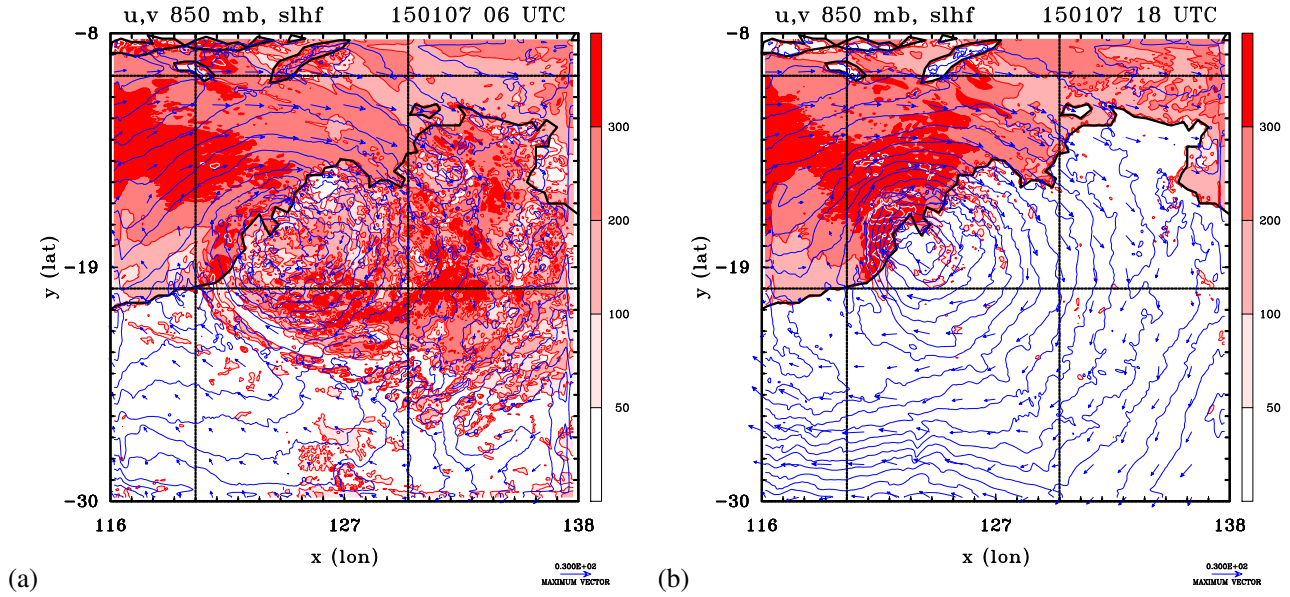

Figure 15. Surface latent flux (shaded), surface pressure and wind vectors at two times: (a) 0600 UTC and (b) 1800 UTC on 7 January, while the low was still strengthening. Unit for heat flux: W m^{-3} as indicated on the colour bar. Contour interval for surface pressure 1 mb, wind vector scale in m s^{-1} indicated by the arrow below the figure.

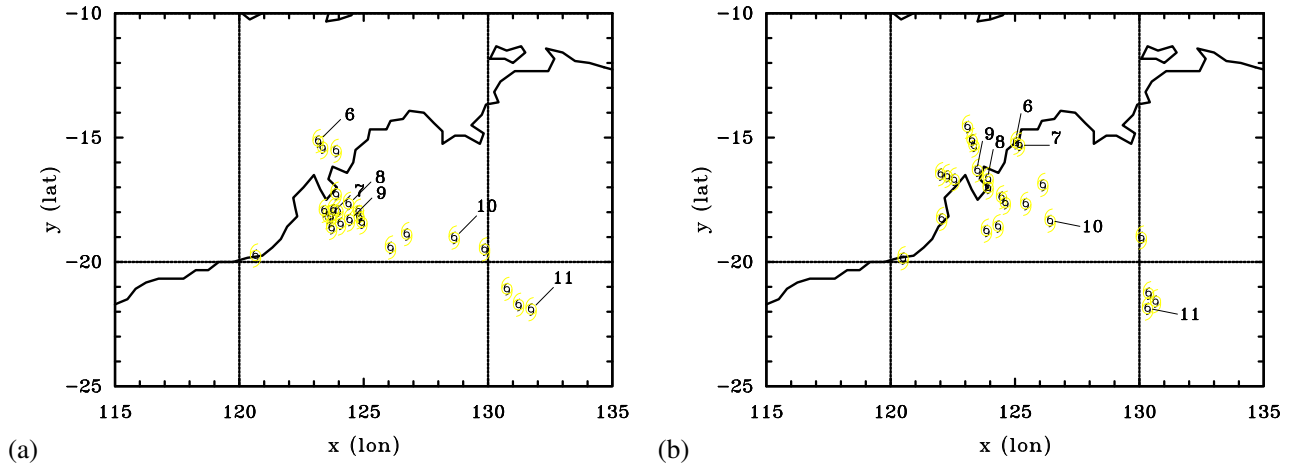

Figure 16. Locations of minimum surface pressure every six hours denoted by a cyclone symbol in (a) the main simulation and (b) the simulation with suppressed surface moisture fluxes over land, starting at 00 UTC 6 January. The locations at 00 UTC are indicated by the day of the month.

intensity is lower in this simulation than in the control simulation, but only slightly and intensification still occurs. Thus there is sufficient moisture available from the sea in the suppressed moisture flux simulation to sustain deep convection. However, it should be pointed out that the centre of the suppressed moisture flux simulation remains a little closer to the coast until after 10 January and at early times the centre is frequently over the sea. This difference in behaviour may be seen in Figure 16, which compares the locations of minimum surface pressure for the two calculations.

It should be noted also that the foregoing behaviour is different from that postulated by Emanuel *et al.* (2008) and that found by Evans *et al.* (2011), presumably due to the proximity of the relatively warm sea in our case.

5 Conclusions

We have presented a case study of an inland low that intensified over land near the northern coast of Western Australia in January 2015. The study was based on European Centre for Medium Range Weather Forecasts (ECMWF) analyses as well as two cloud-permitting, 6-day, limited-area forecasts using the Australian Bureau of Meteorology's UM model with 4 km grid spacing. In one of the UM forecasts, the latent heat flux was suppressed over the land in order to assess the importance of soil moisture on the intensification of the low.

For the first five days, the track and intensity of the low in the UM forecast was in close agreement with those in the ECMWF analyses, but there was a notable departure of the track on the final day of the forecast. The low intensity, characterized by the minimum geopotential height at 850 mb, was slightly deeper in the forecast, a result that would be expected on account of the higher horizontal resolution of the forecast model than of the ECMWF global analyses. The dynamics of low intensification in the UM simulation is shown to be consistent with that in the classical paradigm for tropical cyclone intensification. In this paradigm, convergence in the lower troposphere brought about by the overturning circulation driven by the collective effects of deep convection leads to a concentration of vertical absolute vorticity. As a result of Stokes' theorem, the concentration of vorticity is accompanied by an increase in circulation about fixed closed circuits about the centre of circulation.

It was shown that the mature low had a warm-core structure in the upper troposphere, but a cold-core structure in the lower troposphere, similar to the previously reported structure of the monsoon trough, itself.

In the simulation where the surface latent heat fluxes were suppressed over land, the vortex still intensified and the maximum intensity was only marginally less than in the main simulation. Such behaviour is different from that postulated by Emanuel *et al.* (2008) and that found by Evans *et al.* (2011). However, in this case the centre of circulation was closer to the coast or even just out to sea in the early stages of evolution in the simulation with the latent heat flux suppressed.

6 Acknowledgements

The Australian Government's National Environmental Science Programme (NESP) is acknowledged for their support of this work. We are grateful to colleagues Gerard Kilroy and Mike Montgomery for their perceptive comments on the pre-submission and revised versions of this manuscript.

7 References

Bauer, P., and coauthors, 2011: Satellite cloud and precipitation assimilation at operational NWP centres. *Q. J. R. Meteorol. Soc.*, DOI:10.1002/qj.905

Best, M. J., and coauthors, 2011: The Joint UK Land Environment Simulator (JULES), model description. Part 1: Energy and water fluxes, *Geosci. Model Dev.*, **4**, 677-699.

Boutle, I. A., Abel, S. J., Hill, P. G., and Morcrette, C. J., 2014a: Spatial variability of liquid cloud and rain: observations and microphysical effects, *Q. J. R. Meteorol. Soc.*, **140**, 583-594.

Boutle, I. A., Eyre, J. E. J., and Lock, A. P., 2014b: Seamless stratocumulus simulation across the turbulent gray zone, *Mon. Wea. Rev.*, **142**, 1655-1668.

Bush, M., and coauthors, 2019: The first Met Office Unified Model/JULES Regional Atmosphere and Land configuration, RAL1, *Geosci. Model Dev. Discuss.*, in review.

Clark, D. B., and coauthors, 2011: The Joint UK Land Environment Simulator (JULES), model description Part 2: Carbon fluxes and vegetation, *Geosci. Model Dev.* **4**, 701-722.

Cotton, R. J., and coauthors, 2013: The effective density of small ice particles obtained from in situ aircraft observations of mid-latitude cirrus, *Q. J. R. Meteorol. Soc.*, **139**, 1923-1934.

Davies, H. C., 1976: A lateral boundary formulation for multi-level prediction models, *Q. J. R. Meteorol. Soc.*, **102**, 405-418.

Edwards, J. M. and Slingo, A.,1996: Studies with a flexible new radiation code. I, Choosing a configuration for a large-scale model, *Q. J. R. Meteorol. Soc.*, **122**, 689-719.

Emanuel, K. A., Callaghan, l, J. and Otto, P., 2008: A hypothesis for the redevelopment of warm-core cyclones over northern Australia. *Mon. Wea. Rev.*, **136**, 3863-3872.

Evans, C., Schumacher, R. S. and Galarneau T. J. Jr., 2011: Sensitivity in the overland reintensification of tropical cyclone Erin (2007) to near-surface soil moisture characteristics. *Mon. Wea. Rev.*, **139**, 3848-3870.

Field, P. R., Heymsfield, A. J., and Bansemer, A., 2007: Snow size distribution parameterization for midlatitude and tropical ice clouds, *J. Atmos. Sci.*, **64**, 4346-4365.

Haynes, P. and McIntyre, M. E., 1987. On the evolution of vorticity and potential vorticity in the presence of diabatic heating and frictional or other forces. *J. Atmos. Sci.*, **44**, 828-841.

Hendricks, E. A., Montgomery, M. T. and Davis, C. A., 2004. On the role of 'vortical' hot towers in formation of tropical cyclone Diana (1984). *J. Atmos. Sci.*, **61**, 1209-1232.

Kilroy, G. and Smith, R. K., 2015: Tropical cyclone convection: the effects of a vortex boundary-layer wind profile on deep convection. *Q. J. R. Meteorol. Soc.*, **141**, 714-726.

Kilroy, G., Smith, R. K. and Montgomery M. T. Lynch, B. and Earl-Spurr, C., 2016: A case-study of a monsoon low that formed over the sea and intensified over land as seen in ECMWF analyses. *Q. J. R. Meteorol. Soc.*, **142**, 2244-2255.

Kilroy, G., Smith, R. K. and Montgomery M. T., 2017: Tropical low formation and intensification over land as seen in ECMWF analyses. *Q. J. R. Meteorol. Soc.*, **143**, 772-784.

Lock, A. P., Brown, A. R., Bush, M. R., Martin, G. M., and Smith, R. N. B., 2000: A new boundary layer mixing scheme. Part I: Scheme description and single-column model tests, *Mon. Wea. Rev.*, **128**, 3187-3199.

Love G. B., and G. Garden, 1984: The Australian Monsoon of January 1974. *Aust. Meteor. Mag.*,**32**, 185-194.

McBride, J.L. and Keenan, T.D. 1982. Climatology of tropical cyclone genesis in the Australian region. *J. Clim.*,**2**, 13-33.

Manners, J., Edwards, J. M., Hill, P., and Thelen, J.-C., 2018: SOCRATES (Suite Of Community RAdiative Transfer codes based on Edwards and Slingo), *Technical Guide*, Met. Office, UK, https://code.metoffice.gov.uk/trac/socrates.

May, P., J. Mather, G. Vaughan, C. Jacob, G. McFarquhar, K. Bower and G. Mace,2008: The tropical warm pool international cloud experiment, *Bulletin of the American Meteorol. Soc.*, **89** 629-646.

Montgomery, M. T. and Smith, R. K., 2014: Paradigms for tropical cyclone intensification. it Aust. Meteorol. Ocean. Soc. J. **64**, 37-66.

Montgomery, M. T. and Smith, R. K., 2017: Recent developments in the fluid dynamics of tropical cyclones. *Annu. Rev. Fluid Mech.*, **49**, 541-574.

Montgomery, M. T., Nicholls M. E., Cram, T. A. and Saunders, A. 2006. A 'vortical' hot tower route to tropical cyclogenesis. *J. Atmos. Sci.*, **63**, 355-386.

Ooyama, K. V., 1969: Numerical simulation of the life cycle of tropical cyclones. *J. Atmos. Sci.*, **26**, 3-40.

Perkey, D. J., and Kreitzberg, C. W., 1976: A time-dependent lateral boundary scheme for limited-area primitive equation models, *Mon. Wea. Rev.*, **104**, 744-755.

Persing, J., Montgomery, M. T., McWilliams, J. and Smith, R. K., 2013. Asymmetric and axisymmetric dynamics of tropical cyclones. *Atmos. Chem. Phys.* **13**,12299-12341,

Raymond, D. J., Gjorgjievska, S., Sessions, S. L. and Fuchs, Z., 2014: Tropical cyclogenesis and mid-level vorticity. *Aust. Meteorol. Oceanogr. J.*, **64**, 11-25.

Smith, R. K. and Montgomery, M. T., 2016: The efficiency of diabatic heating and tropical cyclone intensification. *Q. J. R. Meteorol. Soc.*, **142**, 2081-2086.

Smith, R. K., Montgomery, M. T., Kilroy, G., Tang S. and Müller, S. K. 2015: Tropical low formation during the Australian monsoon: The events of January 2013. *Aust. Meteorol. Oceanogr. J.*, **65**, 318-341.

Smith, R. K., Zhang, J. A. and Montgomery, M. T., 2017: The dynamics of intensification in a Hurricane Weather Research and Forecasting simulation of Hurricane Earl (2010). *Q. J. R. Meteorol. Soc.*, **143**, 293-308.

Smith, R. N. B., 1990: A scheme for predicting layer cloud and their water content in a general circulation model, *Q. J. R. Meteorol. Soc.*, **116**, 435-460.

Tang, S., Smith, R. K., Montgomery, M. T. and Gu, M., 2016: Numerical study of the spin up of a tropical low over land during the Australian monsoon. *Q. J. R. Meteorol. Soc.*, **142**, 2021-2032.

Walters, D. N., and coauthors, 2011.: The Met Office Unified Model Global Atmosphere 3.0/3.1 and JULES Global Land 3.0/3.1 configurations, *Geosci. Model Dev.*, **4**, 919-941.

Wilson, D. R. and Ballard, S. P., 1999: A microphysically based precipitation scheme for the UK Meteorological Office Unified Model, *Q. J. R. Meteorol. Soc.*, **125**, 1607-1636.

Wilson, D. R., Bushell, A. C., Kerr-Munslow, A. M., Price, J. D., and Morcrette, C. J.: PC2: A prognostic cloud fraction and condensation scheme. I: Scheme description, 2008, *Q. J. R. Meteorol. Soc.*, , **134**, 2093-2107.

Wissmeier, U. and Smith, R. K., 2011. Tropical-cyclone convection: The effects of ambient vertical vorticity. *Q. J. R. Meteorol. Soc.*, **137**, 845-857.

Wood, N., and coauthors, 2014: An inherently mass-conserving semi-implicit semi-Lagrangian discretization of the deep-atmosphere global non-hydrostatic equations, *Q. J. R. Meteorol. Soc.*, **140**, 1505-1520.

Yang, G. Y., and Slingo, J. M., 2001: The diurnal cycle in the tropics, *Mon. Wea. Rev.*, **129**, 784-801.

